Inorganic Chemistry
Article
pubs.acs.org/IC

Mo- and W-Based Organic Nanostructures Prepared from Bulk Crystal Isomorphs Consisted of $[(CH_3CH_2)_3NH)]_2[MO_2(C_{14}H_6O_4)_2]$ (M = Mo, W)

B. Zhang,[†] S. Z. Du,[†] X. M. Lu,*[,†,‡] G. Wang,[†,‡] and J. Fen[†]

[†]Department of Chemistry, Capital Normal University, Beijing, 100048, China

[‡]State Key Laboratory of Structural Chemistry, Fujian Institute of Research on the Structure of Matter, Chinese Academy of Sciences, Fuzhou, Fujian 350002, China

Supporting Information

ABSTRACT: Two new crystal isomorphs consisting of complexes $[(CH_3CH_2)_3NH)]_2[MoO_2(C_{14}H_6O_4)_2]$ (**1**) and $[(CH_3CH_2)_3NH)]_2[WO_2(C_{14}H_6O_4)_2]$ (**2**) have been synthesized, respectively, and from which Mo-based flexible and durable nanopipes with diameters of 16 nm and lengths of hundreds of micrometers and W-based rigid and fragile nanotubules with ununiform diameters ranging from 30 to 100 nm and lengths in tens of micrometers have been prepared separately, which revealed that the change of the metal in the coordination center of the isomorphs can result in obvious variation to their nanostructures. The crystals both exhibited multilayered structures by the piling of lamellar repeating motifs through van der Waals forces, which are formed by the parallel alignment of 1D chains through hydrogen bonds, and the 1D chains are assembled by complexes **1** and **2**, respectively, through geometrical intercalation and $\pi-\pi$ packing. However, under grinding and ultrasonication, crystal **1** disassembled uniformly into longer and narrower nanostrips, whereas crystal **2** were broken at random into shorter and wider nanoribbons; therefore, the two lamellar nanostructures curled into different cylindrical nanospecies. The differences caused by Mo and W are the following: the Mo complex prefers to assemble into more durable one-dimensional structures along Mo−O bonds than W isomorphs; since Mo−O bonds are weaker than Mo═O and W−O bonds, then the weakest Mo−O bonds can be supported by the adjacent molecules through intercalation and $\pi-\pi$ packing, which resulted in that the linkages among the Mo complexes are stronger along the Mo−O direction and hence the longer Mo-based cylindrical structure. Moreover, the flexibility of Mo-based nanopipes and the rigidity of W-based nanotubules might be attributed to that Mo possesses a lower melting point than W; therefore, Mo is softer and W is harsher.

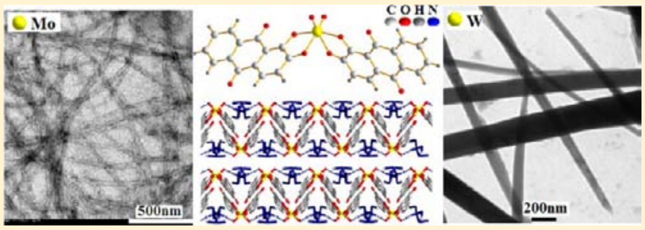

INTRODUCTION

Tenne et al. have reported polyhedral and cylindrical nanostructures assembled with WS_2,[1] a nested fullerene nanostructure integrated with MoS_2 and WS_2,[2] and a cylindrical nanostructure arranged with MoS_2.[3] Continuing, he prepared a series of nanostructures assembled with Mo, W, and other metal inorganic compounds using different methods[4−12] and wrote a review about the progress in metal inorganic nanomaterials.[13] Furthermore, nanoarchitectures, such as nanotubes, nanowires, nanorods, nanobelts, nanolamellas, and nanospheres, have been successfully synthesized,[14−27] especially Mo/W-based nanostructures because of their key role in catalysis, magnetism, optics, and medical science.[28−34] At present, various methods, such as catalytic vapor−liquid−solid growth,[35] direct solid−solid and gas−solid reactions,[36] hydrothermal,[37] and template-based design techniques,[38] have been applied to assemble these architectures, particularly the preparation of the nanostructure from MX_2 (M = Mo and W; X = S, O, and Se).[39−45] However, the controlled preparation of such nanospecies still needs to be developed and the formation mechanisms still need to be clarified.[46] Moreover, in contrast to the Mo/W-based inorganic nanomaterials, the Mo/W-based organic hybrid nanomaterials are seldom reported, due to that the metal organic hybrid materials are easier to be destroyed under higher temperature and crucial experimental conditions, even under the irradiation of the electron beam of TEM. In addition, the differences caused by Mo and W in the formation of the nanomaterials are reported scarcely, of which the reason might be that the differences in inorganic materials are not so obvious. In our previous paper, we have reported a series of nanostructures assembled of complexes $[MoO_2(cat)_2]^{2-}$ and $[WO_2(cat)_2]^{2-}$ with diamines[47,48] and revealed that all the nanomorphologies are associated with the quantum repeating motifs in crystal lattices; however, factors that cause the variation from Mo to W are still blurred. To study the differences caused by Mo and W, herein, we have chosen organic ligand alizarin to combine with Mo and W separately, and obtained two new isomorphic

Received: May 6, 2013
Published: August 5, 2013

crystals consisting of [(CH$_3$CH$_2$)$_3$NH)]$_2$[MoO$_2$(C$_{14}$H$_6$O$_4$)$_2$] (**1**) and [(CH$_3$CH$_2$)$_3$NH)]$_2$[WO$_2$(C$_{14}$H$_6$O$_4$)$_2$] (**2**), respectively; through grinding and ultrasonication, we prepared two noticeably different nanostructures, that is, flexible and durable Mo-based nanopipes with uniform diameters of 16 nm and lengths over hundreds of micrometers, and rigid and fragile W-based nanotubules with ununiform diameters from 30 to 100 nm and lengths in tens of nanometers, and revealed the mechanism of the differences caused by Mo and W in nanostructures, which offered a new method that the metal−organic nanostructures can be designed and prepared from bulk metal complex crystals.

■ RESULT AND DISCUSSION

Molecular and Crystal Structures of Isomorphs 1 and 2. The IR spectra data are listed in Table 1, the summary of parameters of the crystals **1** and **2** for the data collection and refinement is provided in Table 2, selected bond lengths and angles are given in Table 3, and selected hydrogen bonds, π−π packing distances, and van der Waals force distances are listed in Table 4. The single-crystal X-ray diffraction analysis reveals that [(CH$_3$CH$_2$)$_3$NH)]$_2$[MoO$_2$(C$_{14}$H$_6$O$_4$)$_2$] (**1**) and [(CH$_3$CH$_2$)$_3$NH)]$_2$[WO$_2$(C$_{14}$H$_6$O$_4$)$_2$] (**2**) are isomorphic complexes, and both crystallized in a monoclinic system with space group *C*2/*c* as crystal isomorphs. The molecular structure of the two isomorphic complexes are shown in Figure 1A, of which each central metal M (M = Mo or W) coordinated with two alizarins, displaying a cis-dioxo fashion with a chiral pseudo-octahedral [MO$_6$] coordination geometry. In the crystal lattice, the chiral [MO$_2$(C$_{14}$O$_4$H$_6$)2]$^{2-}$ (Λ or Δ) anions parallelly aligned along the *a*, *b*, and *c* axes (Figure 1B,C,D), respectively. Especially, the chiral [MO$_2$(C$_{14}$H$_6$O$_4$)$_2$]$^{2-}$ (Δ or Λ) anions coupled with their enatiomers (Λ or Δ) through geometrical intercalation and π−π packing along the direction perpendicular to the crystal 101 plane in the *ac* plane formed mesomeric one-dimensional (1D) chains. The 1D chains parallelly aligned formed mesomeric lamella in the *ac* plane through hydrogen bonds that are perpendicular to the 1D chains (Figure 1E), and the mesomeric sheet as a quantum repeating motif constituted multilayered structures through van der Waals forces along the *b* axis (Figure 1F). Obviously, the van der Waals force among the layers is the weakest force in crystal lattices; therefore, it can be deduced that the multilayered structures are ready to slip into mono- or nanolamellas similar to multilayered graphite and MX$_2$ (M = Mo and W; X = O and S) structures. Furthermore, if parts of the hydrogen bonds among the 1D chains within the repeating lamella are broken, the lamella can split into narrow nanolamellas and then curl into cylindrical nanostructures. Moreover, if parts of the geometrical intercalation and the π−π packing among the complexes within the 1D chain are destructed, the narrow lamellas can disassemble into shorter ones and then curl into shorter cylindrical nanoarchitectures.

Table 1. Characteristic IR Data (cm^{-1}) of Complexes 1 and 2

assignment	1	2
ν Mo(W)=O	835	838
ν =CH	3040	3024
ν C=C	1535, 1450	1541, 1462
ν C−O	1279, 1250	1278, 1251
ν C=O	1653	1656
ν N−H	3340	3441
γ =C−H	715, 667	716, 669

Table 2. Crystal Data and Structure Refinement of Crystals 1 and 2

crystal	1	2
empirical formula	C$_{40}$H$_{44}$MoN$_2$O$_{10}$	C$_{40}$H$_{44}$WN$_2$O$_{10}$
formula weight	808.71	896.62
temperature	298(2) K	298(2)K
wavelength	0.71073 Å	0.71073 Å
crystal system	monoclinic	monoclinic
space group	*C*2/*c*	*C*2/*c*
a, Å	26.990(3)	27.215(3)
b, Å	10.3670(10)	10.2110(10)
c, Å	13.2831(13)	13.5221(12)
α, deg	90	90
β, deg	92.0280	93.2330(10)
γ, deg	90	90
vol, Å^3	3714.4(6)	3751.7(6)
Z	4	4
calcd density, Mg/m^3	1.446	1.587
Goodness-of-fit on *F*^{2}	1.009	1.349
F(000)	1680	1808
completeness	99.8%	99.6%
final *R* indices [*I* > 2θ(*I*)]	R1 = 0.0454, wR2 = 0.0973	R1 = 0.0404 wR2 = 0.0987
R indices (all data)	R1 = 0.0658, wR2 = 0.1053	R1 = 0.0486 wR2 = 0.1032

Cylindrical Nanostructures Prepared from Bulk Single Crystals 1 and 2, and the Computational Gibbs Free Energies for Complexes 1 and 2 Decomposing into [MoO$_2$]$^{2+}$ or [WO$_2$]$^{2+}$. As deduced above, both of the multilayered crystals disassembled into nanolamellas (Figure 2A), which broke into nanostrips (Figure 2B) and then curled into cylindrical nanostructures (Figures 3 and 4) under grinding and ultrasonication that can generate local temperatures as high as 5000 K and local pressures as high as 500 atm with heating and cooling rates greater than 109 K/s,[28] which can destroy the weak intermolecular interactions, such as the van der Waals force, hydrogen bonds, π−π packing, and geometrical intercalation. Parts of [(CH$_3$CH$_2$)$_3$NH)]$^+$ might be neutralized by the loss of the H$^+$ and then volatilized, and the H$^+$ might be accepted by [MO$_2$(C$_{14}$H$_6$O$_4$)$_2$]$^{2-}$ that becomes [M(OH)$_2$-(C$_{14}$H$_6$O$_4$)$_2$] in the surface of nanostructures. However, it is worthy to emphasize that, within the nanostructures, the chemical composition is the same as in crystals. Figure 3A,B displays the typical transmission electron microscope (TEM) images of flexible Mo-based nanopipes with uniform diameters 16 nm and lengths over a hundred micrometers prepared from bulk single crystal **1** that consisted of [(CH$_3$CH$_2$)$_3$NH)]$_2$-[MoO$_2$(C$_{14}$H$_6$O$_4$)$_2$]. The nanopipes are very long; hence, we can only find three terminal ends, which are exhibited in Figure 3C, after checking a lot of imagines under TEM, revealing that the nanopipes are very durable along their axial direction. Figure 4A,B shows the rigid W-based nanotubules with diameters ranging from 30 to 100 nm and length in tens of micrometers produced from bulk single crystal **2** that consisted of (CH$_3$CH$_2$)$_3$NH)]$_2$[WO$_2$(C$_{14}$H$_6$O$_4$)$_2$], and Figure 4C is the radial cross section of the nanotubules, of which the varied diameters and empty holes are presented.

Table 3. Selected Bond Lengths (Å) and Angles (deg) of complexes 1 and 2

complex **1**	complex **2**
Mo(1)−O(5) 1.718(2)	W(1)−O(5) 1.744(4)
Mo(1)−O(3) 2.008(2)	W(1)−O(1) 1.997(4)
Mo(1)−O(4) 2.135(2)	W(1)−O(2) 2.122(4)
Mo(1)−O(5)#1 1.718(2)	W(1)−O(5)#1 1.744(4)
Mo(1)−O(3)#1 2.008(2)	W(1)−O(1)#1 1.997(4)
Mo(1)−O(4)#1 2.135(2)	W(1)−O(2)#1 2.122(4)
O(5)#1−Mo(1)−O(4) 160.08(10)	O(1)#1−W(1)−O(1) 160.7(2)
O(5)#1−Mo(1)−O(5) 104.33(15)	O(5)−W(1)−O(5)#1 103.7(3)
O(5)−Mo(1)−O(4) 89.77(10)	O(5)−W(1)−O(2)#1 90.09(18)
O(5)#1−Mo(1)−O(3) 87.42(10)	O(5)#1−W(1)−O(1)#1 88.56(18)
O(4)−Mo(1)−O(4)#1 80.54(12)	O(2)#1−W(1)−O(2) 80.1(2)
O(3)−Mo(1)−O(4) 75.34(9)	O(1)#1−W(1)−O(2)#1 75.13(16)

Table 4. Hydrogen Bonds (Å) and Angles (deg), and *d* and *D* of crystals 1 and 2 (Å)

complex	N−H	H···O	∠N−H···O	N···O	d^a	D^b
1	0.910	2.019	162.61	2.901	3.500	10.367
2	0.910	1.944	169.12	2.843	3.512	10.211

[a] The distance of the $\pi-\pi$ packing of crystals **1** and **2**. [b] The distance among the lamellar repeating motifs of crystals **1** and **2**.

However, it is worthy to note that the Mo- and W-based organic hybrid cylindrical nanomaterials presented not only different sizes but also different flexibility, durability, rigidity and fragility. What made the difference? Comparing with the parameters of unit cells of crystal **1** and **2** in Table 2, a (27 Å) > c (13 Å) > b (10 Å), indicating that the linkages along the b axis are the weakest; therefore, both the multilayered crystals are easiest to disassemble along the b axis. Moreover, the cell length d can be represented by the distance between the lamellas, which is represented by D (van der Waals force) in Figure 1F and Table 4, since D_1 (10.367 Å) > D_2 (10.211 Å); hence, the Mo-based multilayered crystals **1** are easier to disassemble into dispersed nanolamellas than the W isomorphic crystal **2**. Furthermore, the hydrogen bonds formed by $[(CH_3CH_2)_3NH)]^+$ and $[MO_2(C_{14}H_6O_4)_2]^{2-}$ among the Mo-based 1D chains (2.019 Å for Mo═O···H−N) are weaker than those of the W-based 1D chains (1.944 Å for W═O···H−N); therefore, Mo-based lamellar motifs are easier to break into narrower nanolamellas, which then curled into finer cylindrical nanostructures, than the W-based lamellas. In addition, the 1D chains are assembled by $[(CH_3CH_2)_3NH)]_2[MO_2(C_{14}H_6O_4)_2]$ through geometrical intercalation and $\pi-\pi$ packing, which can be measured by the distance (d in Table 4)), whereas d_1 (3.500 Å) < d_2 (3.512 Å). The linkages within the Mo-based 1D chain are stronger than those of the W-based isomorphs; hence, the Mo-based cylindrical structures are more durable and longer, whereas the W-based one are more fragile and shorter. In summarizing, the lengths of the cylindrical nanostructure are associated with the geometrical intercalation and $\pi-\pi$ packing within the 1D chains and the diameters are dependent on the hydrogen bonds between the 1D chains, revealing that the small differences in the weak interactions in the crystal lattice can produce noticeable variations in the formation of nanostructures.

The origin that caused the differences in the $\pi-\pi$ packing interaction d_1 (3.500 Å) < d_2 (3.512 Å), hydrogen bonds Mo═O···H (2.019 Å) < W═O···H (1.944 Å) and Mo═O···H−N (2.901 Å) < W═O···H−N (2.843 Å), and van der Waals forces D_2 (10.211 Å) < D_1 (10.367 Å) between Mo and W isomorphs can be attributed to the coordination bonds M−O and M═O further. The bond lengths between metal and coordinated alizarin are $Mo-O_{trans}$ (2.008 Å) > $W-O_{trans}$ (1.997 Å) and $Mo-O_{cis}$ (2.135 Å) > $W-O_{cis}$ (2.122 Å), which resulted in the $\pi-\pi$ packing interaction d_1 of Mo-coordinated alizarin rings being stronger than the d_2 of W-coordinated alizarin, since the longer Mo−O bonds are more effective in geometrical intercalation and $\pi-\pi$ packing between the aromatic alizarin rings than the shorter W−O bonds. The bond length Mo═O (1.718 Å) < W═O (1.744 Å), indicating that the terminal O atoms are more attracted by Mo than by W; hence, the ability of the Mo-coordinated terminal O to form a hydrogen bond with the adjacent 1D is weaker than that of the W-coordinated terminal bond. Therefore, the hydrogen bond length Mo═O···H < W═O···H. Furthermore, the differences in coordination bonds originate from the differences of electron negativity (W: 2.36; Mo: 2.16); therefore, W attracts aromatic ligands more, which results in the coordination bond lengths Mo−O > W−O, which then led to the terminal O atoms being farther from W due to the stereohindrance. Therefore, the bond lengths Mo═O < W═O.

Moreover, we also revealed the mechanism of the formation of the two different nanostructures by the Gaussian 03 program[49] to calculate Gibbs free energies of complexes **1** and **2** decomposing into $[MoO_2]^{2+}$ or $[WO_2]^{2+}$. Scheme 1 show that the relative ΔG are 0 and 16.6 kcal/mol for the Mo and W complexes, respectively, illustrating that the W complex is more stable and difficult to discompose into $[WO_2]^{2+}$ than its Mo isomorphs. Relating the ΔG and their nanoaggregates, it can be concluded that the less stable molecules tend to assemble themselves along their weaker bonds in order to support each other; therefore, the linkages among them are stronger and their nanoaggregates are more durable. We also can explain the nanostructures from coordination bonds directly. For the Mo complexes, the Mo−O bonds (2.008 and 2.135 Å) are much weaker than Mo═O (1.718 Å); therefore, the Mo complexes arranged themselves along the weaker Mo−O bonds, which can be supported by geometrical intercalation and $\pi-\pi$ packing of the alizarin rings from adjacent Mo complexes. In comparison, the differences of the bond lengths between W−O and W═O are less; therefore, the W complexes trend to aggregate themselves along three dimensions.

In addition, the Mo-based nanopipes are flexible, whereas the W-based nanotubules are rigid, which is associated with that Mo as a metal has a lower melting point (2620 °C) and density (10.2 g/cm^3) than W which possesses a melting point of

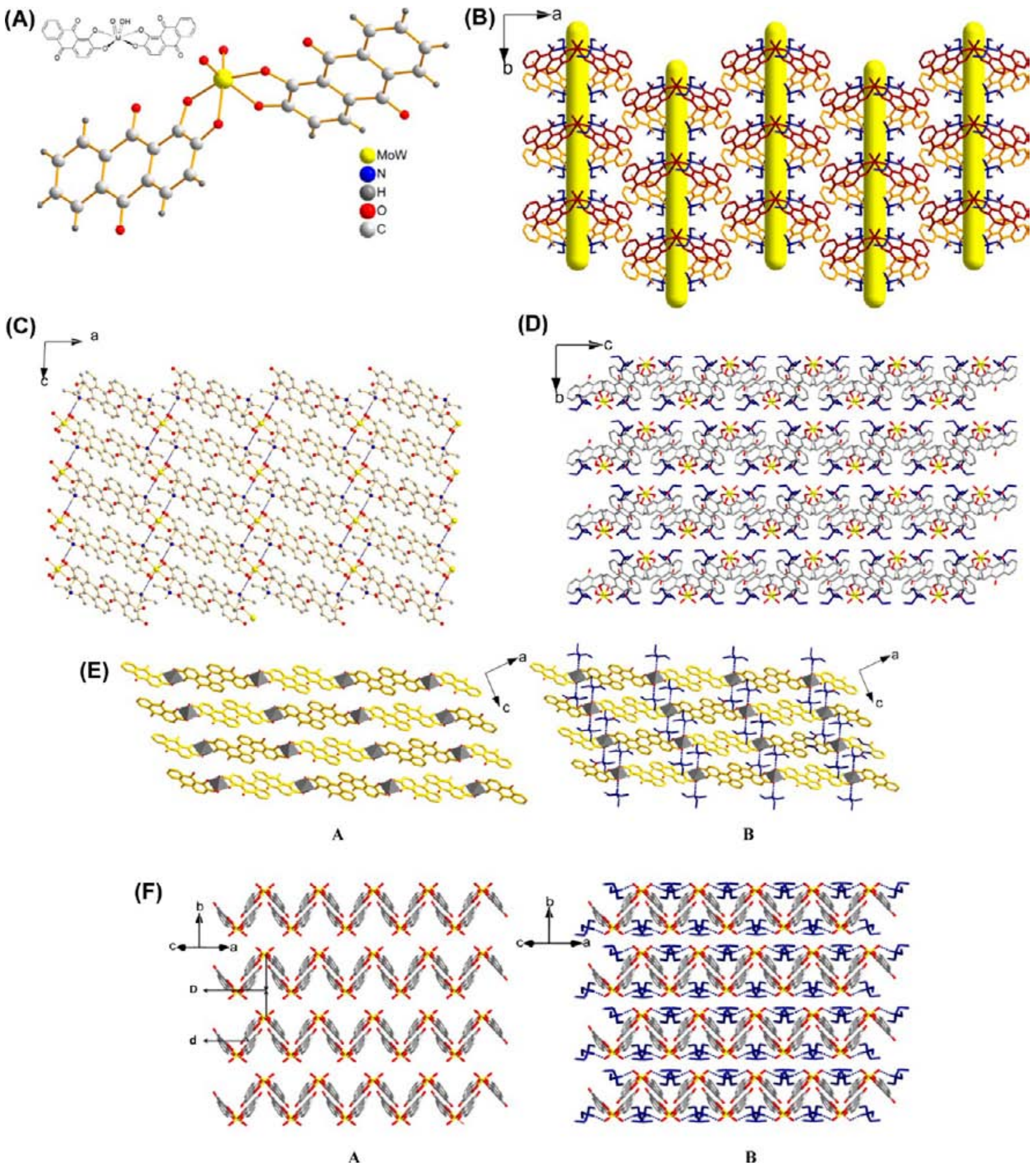

Figure 1. (A) Molecular structure of $[MO_2(C_{14}H_6O_4)_2]$: M = Mo, complex **1**; M = W, complex **2**. (B) The packing of chiral $[(CH_3CH_2)_3NH)]_2[MO_2(C_{14}H_6O_4)_2]$ (M = Mo, complex **1**; M = W, complex **2**) along the *c* axis, of which the same chiral $[MO_2(C_{14}O_4H_6)2]^{2-}$ (Λ or Δ) anions are parallelly aligned along *a* and *b* axes, and $[(CH_3CH_2)_3NH)]^+$ cations shown in blue color are located among the chiral anions. For clarity, the long yellow sticks are added to show the different enantiomeric planes along the *c* axis, and the same color showing the $[MO_2(C_{14}O_4H_6)2]^{2-}$ with the same chirality and located at the same *ab* plane. (C) The packing of $[(CH_3CH_2)_3NH)]_2[MO_2(C_{14}H_6O_4)_2]$ (M = Mo, complex **1**; M = W, complex **2**) along the *b* axis, of which the chiral $[MO_2(C_{14}H_6O_4)_2]^{2-}$ packed with their enantiomers by geometrical intercalation and π−π interaction constituted an infinite mesomeric 1D chain perpendicular to the crystal 101 plane, and the 1D chains are parallelly aligned through hydrogen bonds perpendicular to 1D chains (blue dashed lines) by $[(CH_3CH_2)_3NH)]^+$ cations in the *ac* plane. (D) The packing of $[(CH_3CH_2)_3NH)]_2[MO_2(C_{14}H_6O_4)_2]$ (M = Mo, complex **1**; M = W, complex **2**) along the *a* axis, of which $[MO_2(C_{14}H_6O_4)_2]^{2-}$ anions are linked through π−π interactions between alizarins of the neighboring complexes, which formed mesomeric lamella in the *ac* plane that acted as a repeating motif, constituting a multilayered structure along the *b* axis, and $[(CH_3CH_2)_3NH)]^{\ +}$ cations are shown in blue color. (E) The alignment of 1D mesomeric chains of mesomeric quantum lamella in the *ac* plane that rotated 45° along the *b* axis. A: The chiral $[MO_2(C_{14}H_6O_4)_2]^{2-}$ (Λ or Δ) anions coupled with their enatiomers (Δ or Λ) through geometrical intercalation and π−π packing along the direction perpendicular to the crystal 101 plane in the *ac* plane formed a mesomeric one-dimensional (1D) chain, and the 1D chains parallelly aligned formed mesomeric lamella in the *ac* plane. The $[(CH_3CH_2)_3NH)]^+$ cations are omitted for clarity. B: The hydrogen bonds linked by $[(CH_3CH_2)_3NH)]^+$ cations perpendicular to the chains. (F) The multilayered structure constituted by the mesomeric quantum-lamellar motif. A: The π−π packing interaction distance designated as *d* between alizarins within the mesomeric lamellar repeating motifs and the van der Waals force distance designated as *D* among the lamellar repeating motifs along the *b* axis, of which *d* and *D* are listed in Table 4. For clarity, $[(CH_3CH_2)_3NH)]^+$ are omitted. B: The hydrogen bonds within the mesomeric quantum lamella linked by $[(CH_3CH_2)_3NH)]^+$ cations.

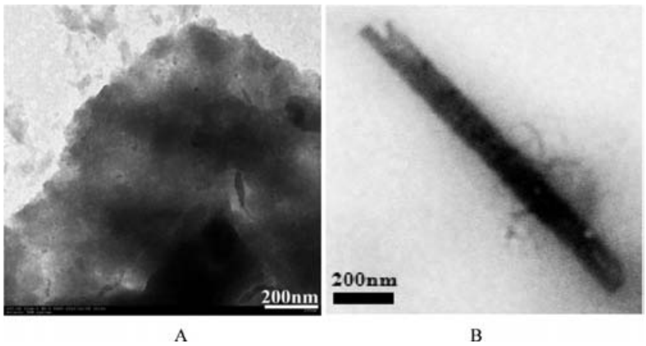

Figure 2. A piece of nanolamella (A) and nanostrip (B) disassembled from the multilayered structure of crystal **2**, from which the curling of the nanolamella and nanostrip can be seen.

3390 °C and a density of 19.35 g/cm^3. In industry, since W metal possesses the highest melting point in the elemental periodic table, then it is harsh; therefore, it is harder to be processed. However, the Mo that has a lower melting point is then softer; hence, it is easier to be treated. For industrial applications, metal Mo is often mixed with W to prepare a Mo−W mixed bialloy for the improvement of the physical properties, especially the flexibility and rigidity; for example, the Mo−W mixed bialloy is more flexible than W, while more rigid than Mo. Similarly, here, the W-based organic hybrid material is more harsh and difficult to be fabricated than Mo isomorphs; therefore, the W-based nanotubules are rigid with diameters in a random scale. In contrast, the Mo-based organic isomorph is softer and easier to be processed; therefore, the Mo-based nanopipes are flexible with uniform diameters.

Comparisons of the PXRD, IR, and Thermogravimetric Analyses of the Bulk Crystals with Their Associated Nanostructures. To confirm the purities of the crystals, the PXRD spectra of the crystals are detected, shown in Figure 5. The experimental and simulated powder X-ray diffraction patterns are almost the same for the Mo-based crystal **1** and W-based crystal **2**, respectively, which illustrated that the crystals **1** and **2** are pure. Furthermore, the PXRD spectra of nanostructures were determined (Figure 5), which are similar to those of their related bulk crystals except that the widths of the peaks are widened and the baselines are not level and smooth, which are due to that the crystallization in nanostructures is less than that in crystals. The same PXRD results of the nanostructures with bulk crystals illustrated that the chemical composition and the linkages among the chemical component are the same in both crystal and nanoaggregate states.

The IR spectra have not presented any obvious differences between the crystals and their associated nanostructures (Figure 6), which indicated that the chemical positions of the

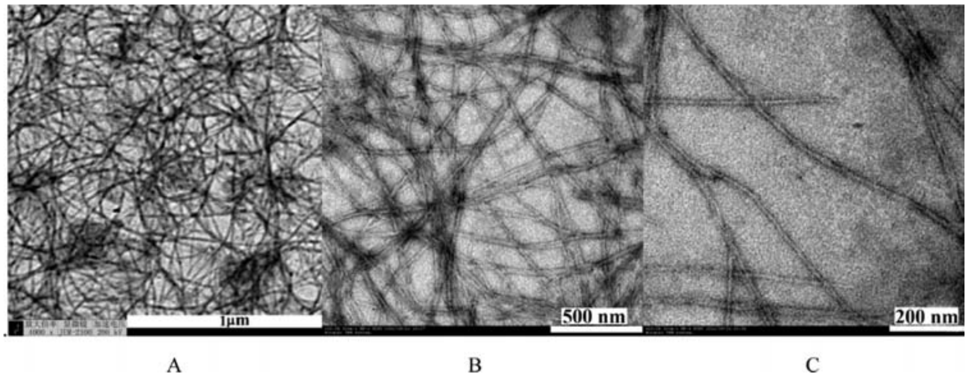

Figure 3. TEM images of the long and flexible nanopipes prepared from crystal **1** that consisted of $[(CH_3CH_2)_3NH)]_2[MoO_2(C_{14}H_6O_4)_2]$. (A, B) The long and flexible nanopipes with diameters of 16 nm and lengths over a hundred μm. Scale bars = 1 μm and 500 nm, respectively. (C) Ten flexible nanopipes from which three terminal ends can be seen. Scale bar = 200 nm.

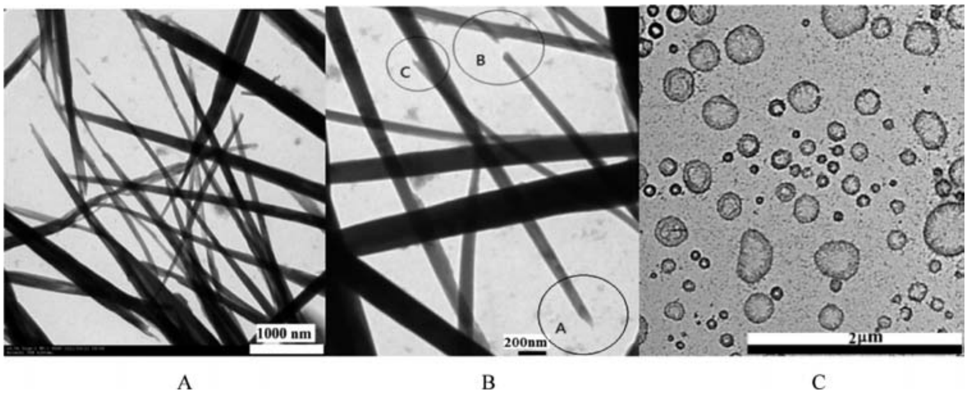

Figure 4. TEM images of the nanotubules prepared from crystal **2** that consisted of $[(CH_3CH_2)_3NH)]_2[WO_2(C_{14}H_6O_4)_2]$. (A) The nanotubules with different diameters and lengths. Scale bar = 1000 nm. (B) The nanotubules with different diameters and lengths, from which the holes are seen from the broken ends of the nanotubule designated by circles A, B, and C. Scale bar = 200 nm. (C) The radial cross sections of the nanotubules with different diameters, of which the different empty holes are presented. Scale bar = 2 μm.

nanostructures are almost the same as with their related bulk crystals.

To study the thermal stabilities of the bulk crystals and nanostructures, and to tell the differences between the Mo-based materials and W-base substances, thermogravimetric analyses are performed with the temperature from zero to 700 °C. The curves of the TG of the bulk crystals are shown in Figure 7, from which we can find that the Mo-based and W-based bulk crystals decomposed from about 202 °C in a 22.1% ratio (calculated ratio is 23.9%) and about 213 °C in a 21.8% ratio (calculated ratio is 21.5%), respectively, which is associated with the thermal decomposition of $(CH_3CH_2)_3NH$ in $[(CH_3CH_2)_3NH)]_2[MoO_2(C_{14}H_6O_4)_2]$, and the Mo-based crystals decomposed at a lower tenmperature than the W-based isomorphs. Furthermore, the Mo-based bulk crystals decomposed from about 528 °C in a 39.7% ratio (the calculated ratio is 57.9%), whereas the W-based decomposed from about 578 °C in a 44.2% ratio (calculated ratio is 52.2%), which are suggested to be attributed to the uncompleted decomposition of $[MoO_2(C_{14}H_6O_4)_2]^{2-}$, and the Mo-based crystals decomposed at lower temperature than the W-based isomorphs. Similarly, the decomposition temperatures of the Mo-based nanostructure are lower than those of the W-based nanostructure. Both of the decomposition temperatures of the W-based bulk crystal and nanostructures are higher than that of the Mo-based isomorphs, which supported the deduction obtained by us that the W-based organic hybrid material is more difficult to be processed; therefore, the W-based nanostructures are rigid and with ununiform diameters, since the melting temperature of W is higher than that of Mo metal. In comparison, the decomposition temperatures of the nanostructures are a little lower than those of their associated crystal, which resulted from that the extent of the crystallization of the nanostructures is less than that of the crystals. The curves of the DTA of the Mo-base and W-based bulk crystals and their nanostructures are shown in Figure 8, which presented also that the decomposition temperatures of the Mo-based materials are lower than those of the W-based isomorphs, and those of the nanostructures are less than those of their related bulk crystals which possessed more crystallization.

■ EXPERIMENTAL SECTION

Materials and Measurements. All reagents were directly obtained from commercial suppliers and were analytical grade without further purification. All manipulations were carried out in the laboratory atmosphere. Single crystal structure determination was performed on a Bruker APEXII area detector device with Mo KR radiation ($\lambda = 0.71073$ Å) by the $\Phi-\omega$ scan method. The transmission electron microscopy (TEM) experiments were recorded on a Hitachi 7650 electron microscope. The PXRD spectra were detected in a Bruker D8 Focus instrument. The IR spectra were recorded with KBr pellets on a Bruker EQUINOX 55 FT-spectrometer in the range of 4000−400 cm^{-1}.

Preparation of $[(CH_3CH_2)_3NH)]_2[MoO_2(C_{10}H_6O_4)_2]$ **(1)**. At room temperature, to a mixed solvent of CH_3OH (5 mL) and DMF (5 mL), $MoCl_5$ (0.137 g, 0.5 mmol) and $Mo(CO)_6$ (0.132 g, 0.5 mmol) were added and stirred for dissolution. Alizarin (0.24 g, 1 mmol) was dissolved into CH_3OH (10 mL) and DMF (10 mL) and 4 mL of triethylamine was added for dehydrogenation. Four hours later, the mixed solution of $MoCl_5$ and $Mo(CO)_6$ was dripped to alizarin. After stirring for 96 h, a dark red solution was obtained and filtered into a tube, and then the filtrate was layered with isopropanol. Ten weeks later, red flake-shaped single crystals were obtained (yield: 42%). Elem. Anal. Calcd: C, 59.41%; H, 5.48%; N, 3.46%. Found: C, 59.58%; H, 5.59%; N, 3.57%.

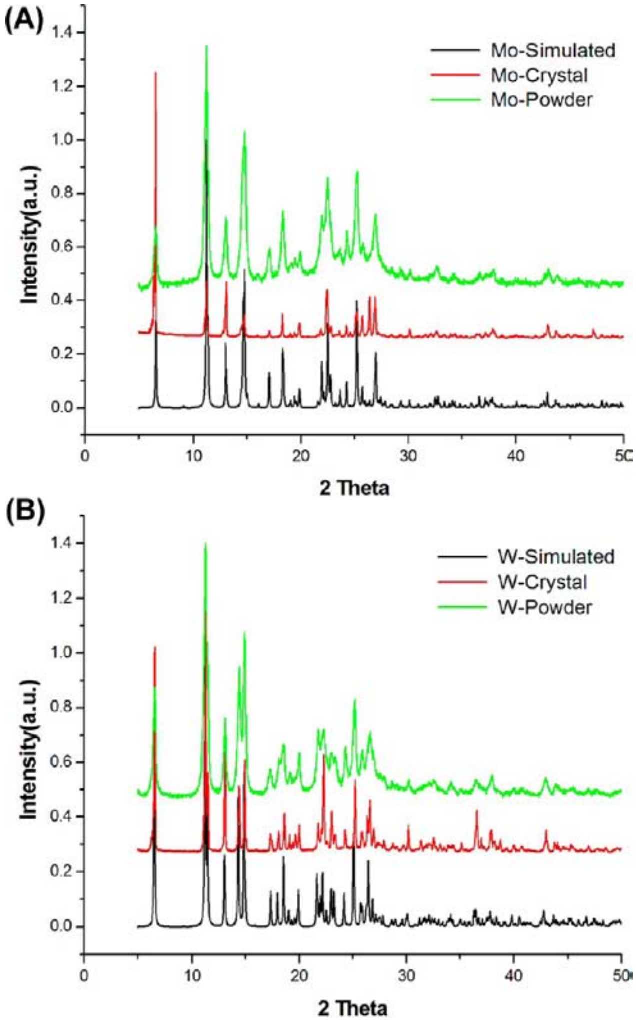

Figure 5. (A) Experimental and simulated powder X-ray diffraction patterns for the molybdenum complex **1**. The black line represents the simulated curves by Mercury from the CIF file (Supporting Information) of the Mo-based single crystal structure, the red line represents the curve of the Mo-based crystal, and the green line represents the curve of the Mo-based nanostructure. (B) Experimental and simulated powder X-ray diffraction patterns for the tungsten complex. The black line represents the simulated curves by Mercury from the CIF (Supporting Information) file of the W-based single crystal structure, the red line represents the curve of the W-based crystal, and the green line represents the curve of the W-based nanostructure.

Preparation of $[(CH_3CH_2)_3NH)]_2[WO_2(C_{10}H_6O_4)_2]$ **(2)**. At room temperature, to a mixed solvent of CH_3OH (5 mL) and DMF (5 mL), WCl_6 (0.2 g, 0.5 mmol) and $W(CO)_6$ (0.176 g, 0.5 mmol) were added and stirred for dissolution. Alizarin (0.24 g, 1 mmol) was dissolved into CH_3OH (10 mL) and DMF (10 mL) and 6 mL of triethylamine was added for dehydrogenation. Four hours later, the mixed solution of WCl_6 and $W(CO)_6$ was dripped to alizarin. After stirring for 96 h, a dark red solution was obtained and filtered into a tube, and then the filtrate was layered with isopropanol. Six weeks later, red flake-shaped single crystals were obtained (yield: 51%). Elem. Anal. Calcd: C, 53.58%; H, 4.95%; N, 3.12%. Found: C, 53.50%; H, 4.88%; N, 3.05%

Infrared Spectra. Using a Bruker EQUINOX55 spectrometer, KBr disks of compounds **1** and **2** were scanned to obtain the infrared spectra, from which the bonding patterns of compounds **1** and **2**

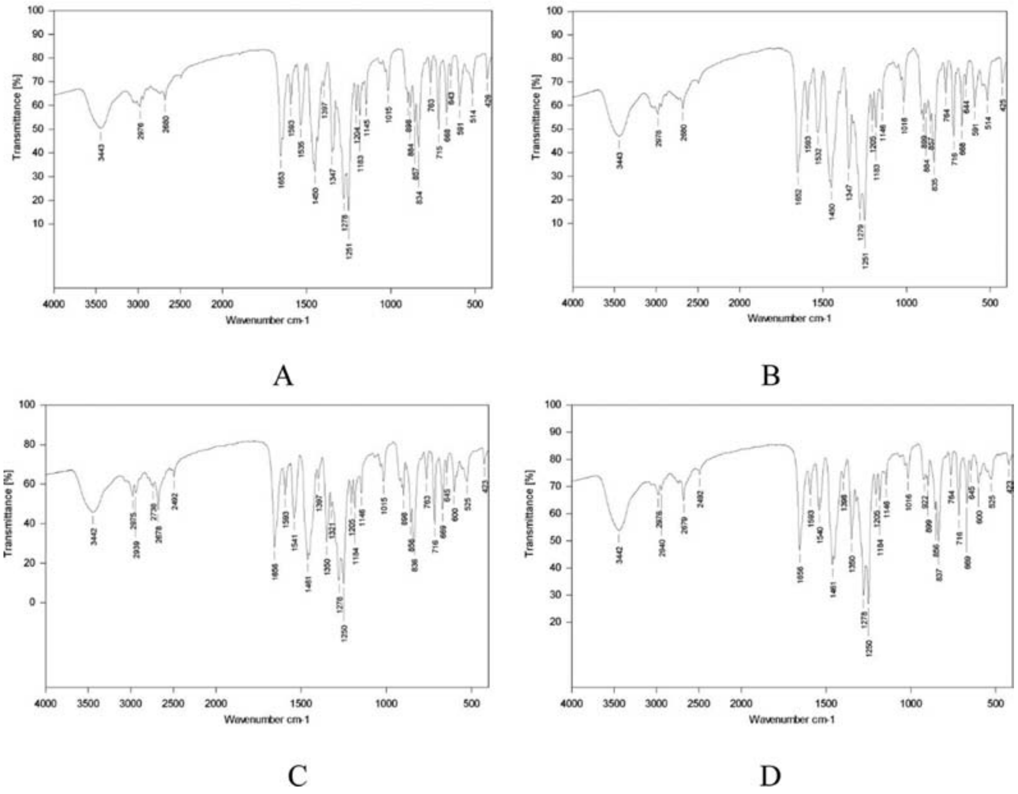

Figure 6. IR spectra of Mo-based crystal **1** (A) and nanostructure (B), and W-based crystal (C) and nanostructure (D).

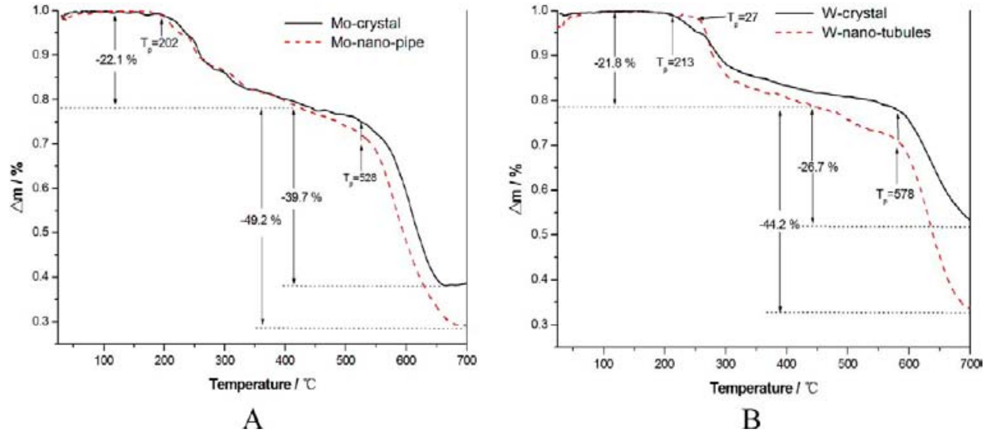

Figure 7. TG curves of the Mo-based crystal **1** and nanostructure (A), and W-based crystal **2** and nanostructure (B).

can be implied. IR spectra of compounds **1** and **2** are summarized in Table 1. We can see that the data are all in the reasonable range, which is consistent with the results of X-ray diffraction. The IR spectra of the nanostructures are the same as the IR spectra of the bulk crystals, which are shown in Figure 6.

X-ray Single-Crystal Determination and Refinement of Crystals 1 and 2. A suitable single crystal was mounted on a glass fiber, and the intensity data collection was carried out with a Bruker Smart APEXII diffractmeter equipped with a CCD detector using Mo−Kα monochromated radiation (λ = 0.71073 Å) at room temperature. The procedure for data reduction was carried out by SAINTPLUS. The structure was solved by direct methods and refined by full-matrix least-squares on F^2 using OLEX2 and SHELXTL-97.[49,50] All non-hydrogen atoms were refined anisotropically. Positions of hydrogen atoms attached to carbon and nitrogen were fixed at their ideal position.

Scheme 1. Calculated Computational Gibbs Free Energies (Δ*G*) from Complexes 1 and 2 to $[MO_2]^{2+}$ (M = Mo, W)

$[Mo^{VI}O_2(C_{14}H_6O_4)_2]^{2-} + 4H^+ \rightarrow [MoO_2]^{2+} + 2C_{14}H_6(OH)_2 \quad \Delta G = 0\ \text{Kcal/mol}$

$[W^{VI}O_2(C_{14}H_6O_4)_2]^{2-} + 4H^+ \rightarrow [WO_2]^{2+} + 2C_{14}H_6(OH)_2 \quad \Delta G = 16.6\ \text{Kcal/mol}$

Preparation of the Nanostructures. Bulk single crystals **1** and **2** were ground into a fine powder separately, and the powders were put into ether. The mixtures were treated by ultrasonication with an ultrasonic cleaner using 40 kHz at room temperature. After 1 h of sonication, the product was checked under TEM.

Computations with Gaussian 03 Program[51] of the Gibbs Free Energies of Complexes. The LYP hybrid density functional was used to fully optimize the structures of compounds **1** and **2**; the pseudo potential Lanl2DZ for the element Mo/W and the 6-31+G(d,p) basis set for the other elements were adopted. The solvent effect was considered through the PCM model.

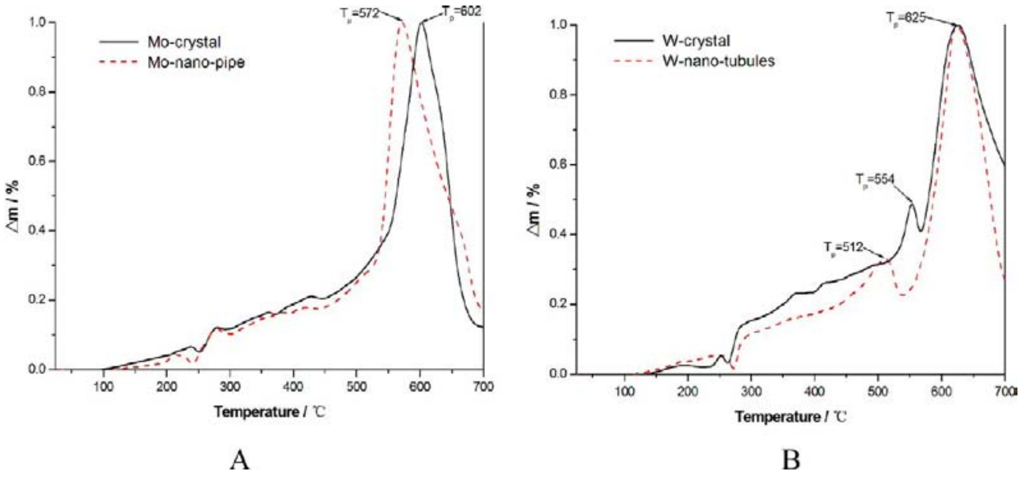

Figure 8. DTA curves of the Mo-based crystal **1** and nanostructure (A), and W-based crystal **2** and nanostructure (B).

CONCLUSION

We have successfully synthesized two new multilayered bulk single crystal isomorphs that consisted of $[(CH_3CH_2)_3NH)][MO_2(C_{14}H_6O_4)_2]$ (**1**: M = Mo; **2**: M = W) by the wet chemical method, and from them, we have manufactured noticeably different Mo/W-based organic hybrid nanostructures by grinding and ultrasonication: long, thinner, flexible, and durable Mo-based nanopipes and shorter, thicker, rigid, and fragile W-based nanotubules. Also, we have revealed the formation mechanism of the different Mo- and W-based cylindrical nanostructures from crystal cell parameters $a > c > b$, and $b_1 > b_2$, $\pi-\pi$ packing distances $d_1 < d_2$, and van der Waals forces $D_1 > D_2$, and the differences of the bond lengths between Mo—O and Mo═O are longer than those between W—O and W═O. We have explained the differences caused by Mo and W from their natural features, such as electronic negativities, melting points, and densities. The PXRD and IR of the nanostructures are almost the same as those of the crystals, which illustrated that the chemical composition in the nanostructure is the same as that in bulk crystals. The decomposition temperatures from the TG and DTA experiments are a little lower for the nanostructures than their bulk crystals, which resulted from that the crystallization of the nanostructures is less than that of bulk crystals. The the decomposition temperatures of Mo-based materials are lower than those of the W-based isomorphs, which are positive to the melting point of Mo and W metals, and illustrated that the W-based organic hybrid material is harder to be processed. Our results offered a new method to prepare the Mo- and W-based organic hybrid nanosubstances from bulk single crystals, which can help others to prepare other metal—organic hybrid nanomaterials that may present different properties from metal inorganic nanomaterials. The different features in metal—organic hybrid nanoarchitectures caused by Mo and W are obviously presented, which might not be noticeable in Mo- and W-based inorganic nanostructures.

ASSOCIATED CONTENT

Ⓢ Supporting Information

CIF files. This material is available free of charge via the Internet at http://pubs.acs.org.

AUTHOR INFORMATION

Corresponding Author

*E-mail: lu-xiaoming@126.com.

Notes

The authors declare no competing financial interest.

ACKNOWLEDGMENTS

We gratefully acknowledge financial support from the Natural National Science Foundation (granted No. 21173150) and the foundation of Fujian Institute of Research on the structure of Matter, Chinese Academy (granted No. 20130007).

REFERENCES

(1) Tenne, R.; Margulis, L.; Genut, M.; Hodes, G. *Nature* **1992**, *360*, 444.

(2) Margulis, L.; Salitra, G.; Tenne, R.; Talianker, M.. *Nature* **1993**, *365*, 113.

(3) Hershfinkel, M.; Gheber, L. A.; Volterra, V.; Hutchison, J. L.; Margulis, L.; Tenne, R. *J. Am. Chem. Soc.* **1994**, *116*, 1914.

(4) Frey, G. L.; Tenne, R.; Matthews, M. J.; Dresselhaus, M. S.; Dresselhaus, G. *J. Mater. Res.* **1998**, *13*, 2412.

(5) Frey, G. L.; Elani, S.; Homyonfer, M.; Feldman, Y.; Tenne, R. *Phys. Rev. B* **1998**, *57*, 6666.

(6) Shahar, C.; Zbaida, D.; Rapoport, L.; Cohen, H.; Bendikov, T.; Tannous, J.; Dassenoy, F.; Tenne, R. *Langmuir* **2010**, *26*, 4409.

(7) Margolin, A.; Gorodnev, A.; Popovitz-Biro, R.; Feldman., Y.; Rapoport, L.; Naveh, G.; Tenne, R. *J. Mater. Chem.* **2009**, *19*, 4368.

(8) Zak, A.; Sallacan-Ecker, L.; Margolin, A.; Genut, M.; Tenne, R. *NANO* **2009**, *4*, 91.

(9) Rosentsveig, R.; Margolin, A.; Feldman, Y.; Popovitz-Biro, R.; Tenne, R. *Chem. Mater.* **2002**, *14*, 471.

(10) Rapoport, L.; Fleischer, N.; Tenne, R. *J. Mater. Chem.* **2005**, *15*, 1782.

(11) Sloan, J.; Tenne, R. *J. Am. Chem. Soc.* **2000**, *122*, 5169.

(12) Frey, G. L.; Tenne, R.; Matthews, M. J.; Dresselhaus, M. S.; Dresselhaus, G. *Phys. Rev. B* **1999**, *60*, 2883.

(13) Luttrell, R. D.; Brown, S.; Cao, J.; Musfeldt, J. L.; Rosentsveig, R.; Tenne, R. *Phys. Rev. B.* **2006**, *73*, 035410.

(14) Alivisatos, A. P. *Science* **1996**, *271*, 933.

(15) Yakobson, B. I.; Smalley, R. E. *Am. Sci.* **1997**, *85*, 324.

(16) Tenne, R.; Margulis, L.; Genut, M.; Hodes, G. *Nature* **1992**, *360*, 444.

(17) Yada, M.; Mihara, M.; Mouri, S.; Kuroki, M.; Kijima, T. *Adv. Mater.* **2002**, *14*, 309.

(18) Ma, R. Z.; Bando, Y.; Zhang, L. Q.; Sasaki, T. *Adv. Mater.* **2004**, *16*, 918.

(19) Siddhartha, S.; Tanmay, B.; Sunil, K. S.; Gajendra, S.; Ramachandrarao, P.; Debabrata, D. *ACS Nano* **2009**, *3*, 1357.

(20) Anil, K.; Yuko, I.; Mitsunori, Y.; Kenichi, N. *J. Am. Chem. Soc.* **2007**, *129*, 1534.

(21) Steven, D. P.; Warren, C. W. C *J. Am. Chem. Soc.* **2009**, *131*, 17042.
(22) Dai, H. J.; Wong, E. W.; Lu, Y. Z.; Fan, S. S.; Lieber, C. M. *Nature* **1995**, *375*, 769.
(23) Jung, H. Y.; Jin, J.; Hyun, M. P.; Sung, B.; Young, W. K; Sung, C. K.; Taeghwan, H. *J. Am. Chem. Soc.* **2005**, *127*, 5662.
(24) Pan, Z. W.; Dai, Z. R.; Ma, C.; Wang, Z. L. *J. Am. Chem. Soc.* **2002**, *124*, 1817.
(25) Pei, Y. K.; Bo, Y. K.; In-Bo, S.; Rabindra, S.; Peter, E. V.; Neal, R. A.; Heemin, Y. *ACS Nano* **2009**, *3*, 3143.
(26) Paritosh, M.; Ilsun, Y.; Taejoon, K.; Kwanyong, S. *J. Am. Chem. Soc.* **2007**, *129*, 9576.
(27) Braun, P. V.; Osener, P.; Stupp, S. I. *Nature* **1996**, *380*, 325.
(28) Vivek, P.; Babita, B.; Rajender, S. V. *ACS Nano* **2009**, *3*, 728.
(29) Li, Y.; Zhou, Z.; Zhang, S.; Chen, Z. *J. Am. Chem. Soc.* **2008**, *130*, 16739.
(30) Ding, Y.; Wan, Y.; Min, Y.-L.; Zhang, W.; Yu, S.-H. *Inorg. Chem.* **2008**, *4*, 7813.
(31) Fiorenzo, V.; Fabio, V.; Paulo, T. O.; Sylvia, F. Z.; Yi, J.-H.; Johannes, S. *Nano Lett.* **2009**, *9*, 659.
(32) Zhang, J.; Soon, J. M.; Lon, K. P. *Nano Lett.* **2007**, *7*, 2370.
(33) Bertolazzi, S.; Krasnozhon, D.; Kis, A. *ACS Nano* **2013**, *7*, 3246.
(34) Liu, G.; Zhang, G. J.; Jiang, F.; Ding, X. D.; Sun, Y. J.; Sun, J.; Ma., E. *Nat. Mater.* **2013**, *12*, 344.
(35) Kiely, C. J.; Fink, J.; Brust, M.; Bethell, D.; Schiffrin, D. J. *Nature* **1998**, *396*, 444.
(36) Penn, R. L.; Banfield, J. F. *Science* **1998**, *281*, 969.
(37) Lou, X. W.; Zeng, H. C. *Chem. Mater* . **2002**, *14*, 4781.
(38) Cui, Y.; Lieber, C. M. *Science* **2001**, *291*, 851.
(39) Liu, J.; Sasidharan, M.; Liu, D.; Yokoyama, Y.; Yusa, S.-i.; Nakashima, K. *Mater. Lett.* **2012**, *66*, 25.
(40) Enyashin, A. N.; Yadgarov, L.; Houben, L.; Popov, I.; Weidenbach, M.; Tenne, R.; Bar-Sadan, M.; Seifert, G. *J. Phys. Chem. C* **2011**, *115*, 24586.
(41) Ramakrishna Matte, H.; Gomathi, A.; Manna, A.; Late, D.; Datta, R.; Pati, S.; Rao, C. *Angew. Chem., Int. Ed.* **2010**, *49*, 4059.
(42) Ishijima, Y.; Kurishita, H.; Arakawa, H.; Hasegawa, M.; Hiraoka, Y.; Takida, T.; Takebe, K. *Mater. Trans.* **2005**, *46*, 568.
(43) Zhu, Y. Q.; Sekine, T.; Li, Y. H.; Fay, M. W.; Zhao, Y. M.; Poa, C. H. P.; Wang, W. X.; Roe, M. J.; Brown, P. D.; Fleischer, N.; Tenne, R. *J. Am. Chem. Soc.* **2005**, *127*, 16263.
(44) Shi, Y. F.; Wan, Y.; Zhao, D. Y.; et al. *J. Am. Chem. Soc.* **2007**, *129*, 9522.
(45) Denny, N. R.; Li, F.; Norris, D. J.; Stein, A. *J. Mater. Chem.* **2010**, *20*, 1538.
(46) Puntes, V. F.; Krishnan, K. M.; Alivisatos, A. P. *Science* **2001**, *291*, 2115.
(47) Lu, X.; Shi, X.; Min, T. *Inorg. Chem.* **2011**, *50*, 2175.
(48) Du, S. Z.; Lu, X. M.; Feng, J.; Cheng, Y. F.; An, L.; Sun, X. J. *CrystEngComm* **2012**, *14*, 6618.
(49) OLEX^2: A Complete Structure Solution, Refinement and Analysis Program. Dolomanov, O. V.; et al. *J. Appl. Crystallogr.* **2009**, *42*, 339.
(50) Sheldrick, G. M. *SHELXTL-97 V5.10*; Bruker AXS Inc.: Madison, WI, 1997.
(51) Frisch, G. W.; Trucks, H. B.; Schlegel, G. E.; Scuseria, M. A.; Robb, J. R.; Cheeseman, J. A.; Montgomery, T., Jr.; Vreven, K. N.; Kudin, J. C.; Burant, J. M.; Millam, S. S.; Iyengar, J.; Tomasi, V.; Barone, B.; Mennucci, M.; Cossi, G.; Scalmani, N.; Rega, G. A.; Petersson, H.; Nakatsuji, M.; Hada, M.; Ehara, K.; Toyota, R.; Fukuda, J.; Hasegawa, M.; Ishida, T.; Nakajima, Y.; Honda, O.; Kitao, H.; Nakai, M.; Klene, X.; Li, J. E.; Knox, H. P.; Hratchian, J. B.; Cross, V.; Bakken, C.; Adamo, J.; Jaramillo, R.; Gomperts, R. E.; Stratmann, O.; Yazyev, A. J.; Austin, R.; Cammi, C.; Pomelli, J. W.; Ochterski, P. Y.; Ayala, K.; Morokuma, G. A.; Voth, P.; Salvador, J. J.; Dannenberg, V. G.; Zakrzewski, S.; Dapprich, A. D.; Daniels, M. C.; Strain, O.; Farkas, D. K.; Malick, A. D.; Rabuck, K.; Raghavachari, J. B.; Foresman, J. V.; Ortiz, Q.; Cui, A. G.; Baboul, S.; Clifford, J.; Cioslowski, B. B.; Stefanov, G.; Liu, A.; Liashenko, P.; Piskorz, I.; Komaromi, R. L.; Martin, D. J.; Fox, T.; Keith, M. A.; Al-Laham, C. Y.; Peng, A.;.Nanayakkara, M.; Challacombe, P. M. W.; Gill, B.; Johnson, W.; Chen, M. W.; Wong, C.; Gonzalez; Pople, J. A. *Gaussian 03*; Gaussian, Inc.: Wallingford, CT, 2004.